Composites Part B 239 (2022) 109950

Contents lists available at ScienceDirect

Composites Part B

journal homepage: www.elsevier.com/locate/compositesb

Geometrical optimization of thermoforming continuous fibers reinforced thermoplastics with Finite Element Models: A case study

Carmelo Gómez [a], Daniel Tobalina-Baldeon, Ph.D. [b], Francisco Cavas, Ph.D. [c,*], Felix Sanz-Adan, Ph.D. [b]

[a] International School of Doctorate, Technical University of Cartagena, 30202, Cartagena, Spain
[b] Department of Mechanical Engineering, University of La Rioja, 26004, Logroño, Spain
[c] Department of Structures, Construction and Graphical Expression, Technical University Cartagena, 30202, Cartagena, Spain

ARTICLE INFO

Keywords:
CFRTPs
FEM
Gear mount
CFRTP Forming process
Tsai's modulus

ABSTRACT

The manufacturing of thermoformed components of continuous fiber-reinforced thermoplastics (CFRTPs) relies on an optimization process owing to a demand for quality and the mechanical requirements. Geometrical optimization is typically based on trial-and-error processes, and delays due to the manufacturing of different prototypes increases the development cost of the final product. In this study, the mechanical behavior of a CFRTPs top mount damping component made of polyamide 6 (PA6) reinforced with long glass fibers (47% in volume) and installed in an automobile differential system was evaluated. This was achieved by developing ad hoc tooling for axial testing. The experimental results were used to validate those obtained using a finite element (FE) model based on the fabricated geometry and mechanical properties of the CFRTPs laminate. Furthermore, a complete mathematical procedure was implemented to address the lack of information on the mechanical moduli and Poisson's ratio in the material datasheet for the FE simulation. This method was based on a Halpin-Tsai model and classical lamination theory with a 3D expansion for out-of-plane mechanical property calculation, wherein Tsai's modulus was obtained for checking purposes. The obtained results were fitted with the test results to validate the developed FE model. In addition, this model was used to further optimize the component geometry. The implementation of in silico models based on FE techniques can be useful for accelerating the development of recyclable CFRTPs for large-scale production, allowing significant weight reduction and lower greenhouse emission without diminishing their reliability and safety throughout their useful life.

1. Introduction

The Paris Agreement on Climate Change established a 90% reduction in global greenhouse gas (GHG) emissions by 2050, compared with levels reached in 1990. The transport sector produced 24.6% of the total emissions in EU [1], with road transport being the biggest contributor to pollution accounting for almost half of this emission. This percentage can be drastically reduced by introducing new types of vehicles.

The development of eco-friendly vehicles is related to the manufacturing of lighter and recyclable structures. Thus, composite components made of continuous fiber-reinforced thermoplastics (CFRTPs) have been steadily growing. Furthermore, their good anti-vibration behavior, high specific stiffness, and strength, in addition to the possibility of using them to develop new architectures [2,3], have accelerated their investigation and application in primary structures in which safety is a key factor. CFRTP components exhibit good strain energy absorption, which depends on the impact velocity [4].

Components manufactured with CFRTPs improve comfort because of their dynamic advantages when they are used as antivibration and damping elements, such as connecting rods and top mounts, as demonstrated by Tobalina-Baldeon D. et al. [5] (Fig. 1). Complex geometries can be thermoformed in these components, enabling the possibility of local reinforcement introduction, metal component insertion, and component mass reduction. The obtained components exhibited good adhesion to vulcanized rubber [6], and the metal insertion increased the bolted preloads and durability of the bolted connections along with considerable mass reduction [7]. The data obtained complemented the values included in the material datasheet.

However, there is a lack of information about the mechanical

* Corresponding author.
E-mail addresses: gomezgarciacarmelo@gmail.com (C. Gómez), Daniel.tobalina@aurea.unirioja.es (D. Tobalina-Baldeon), francisco.cavas@upct.es (F. Cavas), felix.sanz@unirioja.es (F. Sanz-Adan).

https://doi.org/10.1016/j.compositesb.2022.109950
Received 16 January 2022; Received in revised form 29 April 2022; Accepted 29 April 2022
Available online 14 May 2022

Nomenclature

CFRTPs	Continuous fiber reinforced thermoplastics
CLT	Classic Lamination Theory
EU	European Union
GHG	Greenhouse Gases
TEPEX PA6/47 102	TEPEX® dynalite 102-RG600(x)/47 – PA6-GF67 Multi-directional tape

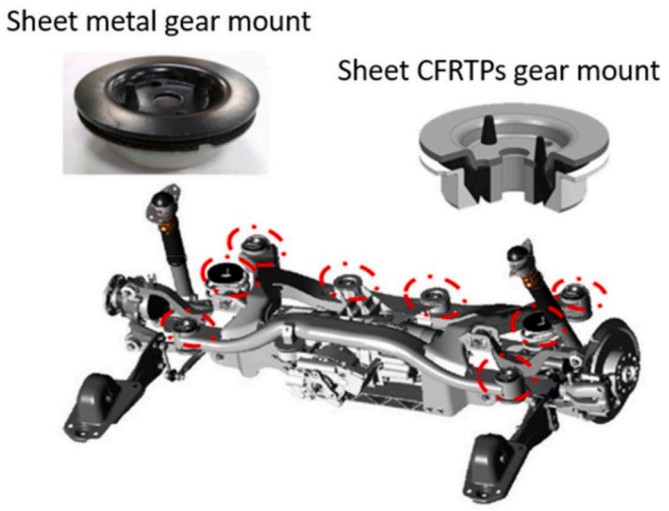

Fig. 1. Illustration of a differential system with antivibration metal and CFRTPs top mount.

properties that hinder the optimization process in finite element (FE) simulation of CFTRPs. In particular, because of the non-isotropic behavior of CFTRPs components, mechanical properties and strengths are required in all directions to evaluate each layer of the laminate or the whole laminate using equivalent properties.

As obtaining material properties using testing is time-consuming and costly, simplified methodologies have been proposed to reduce the number of tests required for mechanical property calculations and the implementation of failure criteria [8]. Therefore, it is crucial to optimize the complex manufacturing processes and ensure that mechanical properties present data with less dispersion.

To address this problem, simple 2D mathematical models have been implemented from a microscale perspective [9] in conjunction within silico models to evaluate different stacking sequences and textile arrangements using unit cell definition [10]. The development of a complete 3D methodology for component analysis with FE models is needed; however, this is hindered by the dependency of the material's properties on fiber orientation [11], matrix viscoelastic behavior, and hydrothermal conditions [12].

The evaluation of fiber orientation, particularly in complex geometries, is a key factor in the manufacturing process of CFRTPs components, which are typically based on thermo-stamping techniques with several trial-and-error processes. For this purpose, Chen et al. [13] developed a numerical algorithm based on an arbitrary Lagrangian-Eulerian (ALE) description to simulate the compression-stamping process by comparing the in silico and experimental tests and obtained accurate results. Zhang et al. [14] proposed a hybrid lamination model to simulate the thermo-stamping of woven fabric-reinforced thermoplastic composites.

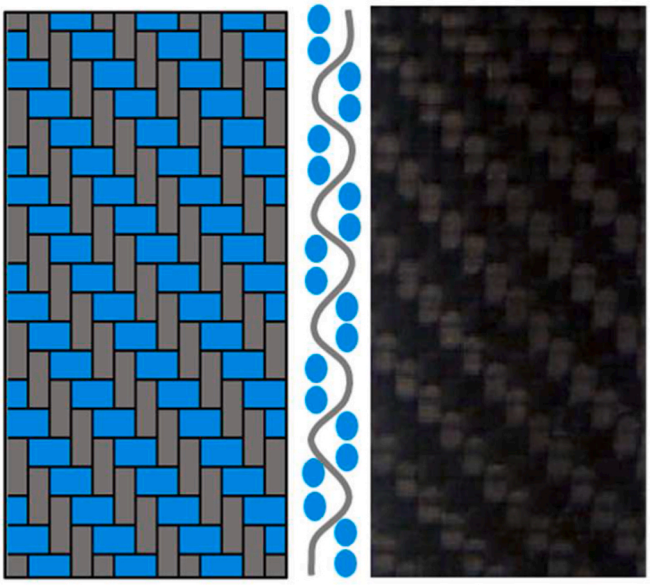

Fig. 2. Scheme of twill weave configuration in the TEPEX® dynalite 102-RG600(x)/47 – PA6-GF67 multi-directional layer and a photograph showing the tape detail.

In silico geometrical optimization has enabled the development of new CFRTPs architectures for structural applications. Zhang et al. [15] developed and analyzed a novel panel concept based on a bendable metal-based composite sandwich structure with a truncated dome core made of CFRTPs. Moreover, they optimized the percentage and dimensions of domes and ply thickness to obtain curved panels.

The use of a thermoplastic matrix in an assembly allows joints to be welded using ultrasonic, laser, or friction procedures, and several studies have focused on [16–19] improving the quality of the joints obtained. Although considerable efforts have been made to obtain joints using the material heating process, bolted connections continue to be the most common joint type, owing to the possibility of replacing components and inspection procedures [20,21].

Composite materials are extensively used in the aerospace industry and account for over 50% of the total mass of recent aircraft models [22]. By contrast, their application in the automotive industry has been limited to high-end and racing cars with monocoque structures [23]. The development of new composite structures for middle-range cars has been restricted to non-structural components such as dashboards, leaf springs, and rear-view mirrors using short-fiber composites.

The incorporation of CFRTPs opens a new horizon for composite applications in primary structures. Several studies have focused on simplifying their manufacturing process. For instance, Tsai et al. [24,25] introduced a double-double composite layup. Furthermore, the component cost must be considered along with the optimal material combination [26].

In this study, a complete and reliable methodology for the design of real automotive components is proposed. For this purpose, a FE model of a CFRTPs core gear mount made of polyamide 6 (PA6) reinforced with long glass fibers (47% in volume) is developed.

The material properties were calculated using the Halpin-Tsai model and classical lamination theory (CLT). The proposed methodology could

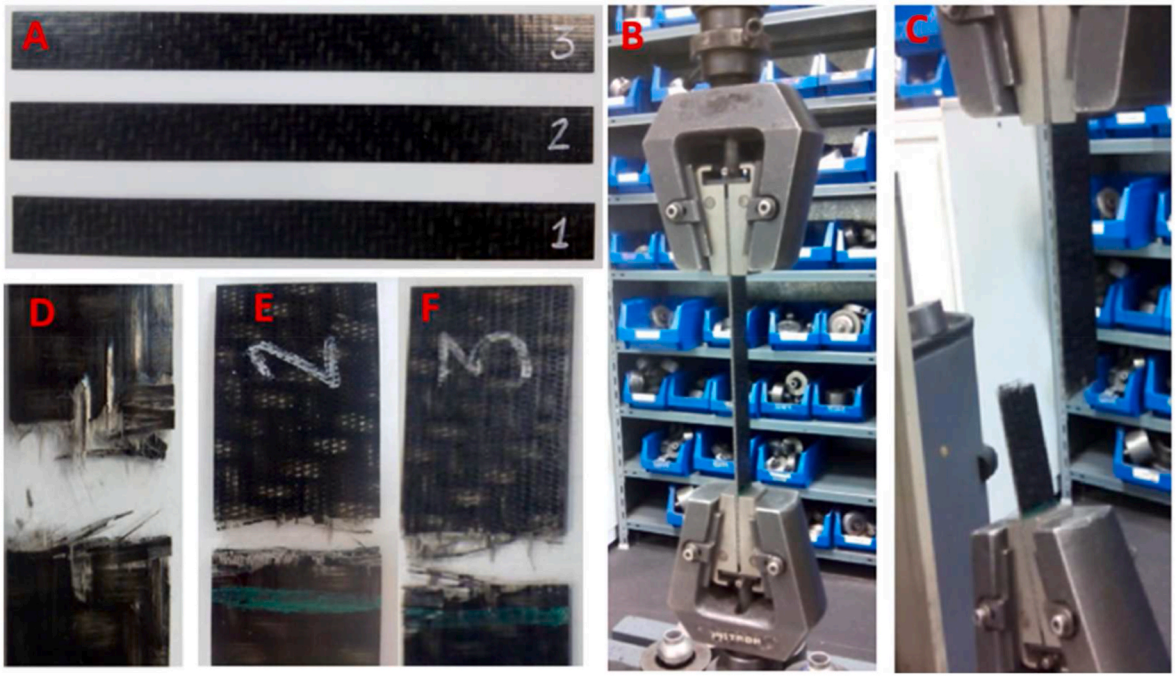

Fig. 3. Tension test of PA6/47 coupons. Coupon tested (A), image of clamping in universal testing machine ZWICK©- serie 1000 (B), image of failure in test coupon 1 (C), and detail images of the failure mode in test coupons (D, E and F).

address the lack of information regarding the mechanical properties required to simulate CFRTPs materials.

The results obtained with the FE model were found to be consistent with and the test results, allowing further optimization to reduce the mass of the component. The results of this study can help avoid the manufacturing of prototypes, which is costly-and time-consuming. Furthermore, the development of validated FE models enables further geometrical optimization processes to obtain lighter and stronger structures.

2. Methods, materials, and experimental methodologies

2.1. Material definition

The CFRTPs core gear mount was fabricated using the commercial layer TEPEX® dynalite 102-RG600(x)/47 – PA6-GF67 multi-directional layer (LANXEXX Deutschland GmbH, Cologne, Germany). Each layer had a nominal thickness of 0.5 mm and was made of Polyamide 6 reinforced with E-glass roving 1200 tex with a twill weave configuration (Fig. 2). The fiber volume content was 47% and the nominal total

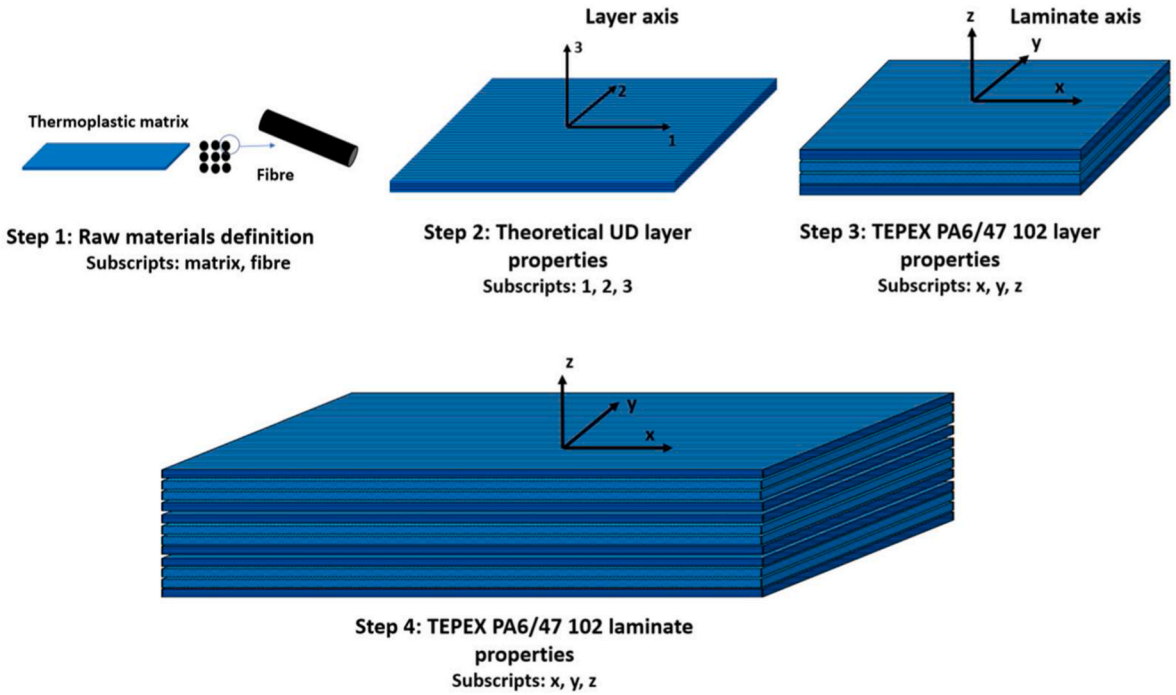

Fig. 4. Calculation procedure for laminate material properties along axis definition and nomenclature.

Table 1
Average properties for raw materials: polyamide 6 (PA6) and E-glass Fiber.

Raw Materials Average Properties		E-Glass Fiber		Polyamide 6 (PA 6)
Young's Modulus (MPa)	E_{fiber}	74 500	E_{matrix}	2995
Poisson's Coefficient (−)	ν_{fiber}	0.21	ν_{matrix}	0.28
Shear Modulus (MPa)	G_{fiber}	30 790	G_{matrix}	1170
Density (kg/m^3)	ρ_{fiber}	2540	ρ_{matrix}	1140

density was 1800 kg/m^3. In this study, the material is referred to as TEPEX PA6/47 102.

2.2. Material test

PA6/47 102 was tested in an axial test according to ISO 527–4 which specifies the test conditions for isotropic orthotropic fiber-reinforced plastic composites. For this purpose, 3 samples with a total length of 250 mm, width of 25 ± 0.5 mm, and nominal thickness of 2 mm were prepared and tested in a universal testing machine (-ZWICK©- serie 1000, Zwick Roell Group, Ulm, Germany) with a maximum load capacity of 100 kN.

Tensile test coupons were clamped using INSTRON 3 and Serie 2716 grips (Instron, Massachusetts, USA) with a total length of 150 mm ± 1 mm. An extension test was performed at a velocity of 2 mm/min.

The average Young's modulus, strength, and strain obtained in the axial test (Appendix A: tension test results correlation) are close to the values in the material datasheet under dry conditions (E = 23 GPa, σ_u = 390 MPa, and ε_u = 2.2% were used in the study). The difference can be attributed to the dispersion of data obtained in tests due to manufacturing process and environmental conditions [27]. As is evident from Fig. 3, coupons 2 and 3 failed close to the grip. This could be attributed to the stress concentration due to the load transfer between the coupon and clamping zone via interlaminar shear stresses, and the concentration due to the in-plane necking zone owing to the non-homogeneous distribution of fibers oriented in both directions.

2.3. Estimation of material mechanical properties estimation and empirical theory

There is a lack of information on the mechanical moduli and Poisson's ratio required for the static analysis of a CFRTPs layer, and not all the parameters required for the static analysis simulation are provided in the material datasheet. For a single layer or laminate, the values of Young's modulus, shear modulus, and Poisson ratios in all directions must be calculated from the test results or theoretical models. In this study, the mechanical properties required for the FE simulation were obtained using the raw material according to the procedure shown in Fig. 4, wherein the axis nomenclature is defined. The mechanical properties of a theoretical unidirectional (UD) layer were calculated from the raw material properties (Step 1) based on a simple rule of mixture and the implementation of the Halpin-Tsai model (Step 2). Each twill-weave layer of the TEPEX PA6/47 102 material was assumed to comprise a combination of theoretical UD layers disposed at 0° and 90° with a symmetrical configuration, with the hypothesis that there is no interaction between the fiber families (Step 3). The mechanical properties of a layer made of TEPEX PA6/47, and the mechanical properties of laminates fabricated from these layers were calculated using lamination theory and a rule of mixture for the out-of-plane mechanical properties. The in-plane Young's moduli in the X-and Y-directions calculated for a single layer were validated by comparing them with the values provided in the material datasheet.

Table 2
Mechanical properties of a theoretical unidirectional layer of Polyamide 6 reinforced with long glass fiber (47% in volume) calculated using rule of mixture and Halpin-Tsai theory.

Density (kg/m^3)	1800
E_1 (MPa)	36 240
E_2 (MPa)	9380
E_3 (MPa)	9380
G_{12} (MPa)	2780
G_{13} (MPa)	2780
G_{23} (MPa)	3225
ν_{12}	0.30
ν_{13}	0.30
ν_{23}	0.46

The calculation procedure for single layer of TEPEX PA6/47 102 is as follows.

The average material properties of the raw material used in the layers is listed in Table 1. These values are based on typical values reported in the literature [28–30].

The properties of the layer were obtained from the mechanical properties of the raw materials according to the Halpin-Tsai model [31] and Hull and Clyne [32], based on the hypothesis that each layer is built with symmetrical individual unidirectional layers at 0° and 90° angles (fiber interaction in the twill weave configuration was not considered).

Young's modulus in the fiber direction E_1 and the mayor Poisson's ratio ν_{12} were calculated using Equations (1) and (2), which are expressed in the form of a simply rule of mixture.

Here, f = 0.47 is the ratio between the volume fiber fraction and total volume, E_{fiber} is the Young's modulus of the fiber, E_{matrix} is the Young's modulus of the matrix, $\nu_{12\ fiber}$ is the major Poisson ratio of the fiber, and $\nu_{12\ matrix}$ is the major Poisson ration of the matrix.

$$E_1 = f \cdot E_{fiber} + (1-f) \cdot E_{matrix} \tag{1}$$

$$\nu_{12} = f \cdot \nu_{fiber} + (1-f) \cdot \nu_{matrix} \tag{2}$$

Young's modulus in the direction perpendicular to fibers E_2 and shear modulus in plane G_{12} were calculated using Equations (3) and (4).

$$E_2 = E_{matrix}\left(\frac{1+\zeta_{E_2}\cdot\eta_{E_2}\cdot f}{1-\eta_{E_2}\cdot f}\right), \tag{3}$$

$$G_{12} = G_{matrix}\left(\frac{1+\zeta_{G_{12}}\cdot\eta_{G_{12}}\cdot f}{1-\eta_{G_{12}}\cdot f}\right), \tag{4}$$

where η_{E_2} and $\eta_{G_{12}}$ are empirical parameters that consider the relationship between the corresponding fibers and matrix modulus, whereas ζ_{E_2} and $\zeta_{G_{12}}$ are empirical corrector factors that consider the geometry of the reinforcement used and the fiber volume fraction [33]. The expressions used for the parameter calculations can be found in Appendix B (material parameter calculation).

According to Hull and Clyne [32], the value of the transverse shear modulus in the plane perpendicular to the fibers direction G_{23} can be expressed as follows.

$$G_{23} = \left(\frac{E_2}{2\cdot(1+\nu_{23})}\right), \tag{5}$$

where the Poisson's ratio in the plane perpendicular to the fiber, ν_{23}, was obtained using Equation (6).

$$\nu_{23} = 1 - \nu_{21} - \frac{E_2}{3K}, \tag{6}$$

where ν_{21} is the minor Poisson ratio, which can be obtained from the definition of the major Poisson ratio expressed in Equation (2) using Equation (7), and K is the bulk modulus. The expression for the calculation of the bulk modulus can be found in Appendix B (material parameter calculation).

$$\nu_{21} = \left(f \cdot \nu_{fiber} + (1-f) \cdot \nu_{matrix}\right) \cdot \frac{E_2}{E_1} \tag{7}$$

The mechanical properties of the theoretical orthotropic layer can be obtained using Equations (1)–(7) with the assumption that for orthotropic layers E_1, $E_2 = E_3$, $G_{12} = G_{13}$, G_{23}, $\nu_{12} = \nu_{13}$, and ν_{23}. The theoretical properties of the UD layer are listed in Table 2.

The density ρ was obtained from a simple rule of mixtures, as can be observed in Equation (8), considering the density of fiber ρ_{fiber} and matrix ρ_{matrix}. In this study, the void content is assumed to be negligible.

$$\rho = f \cdot \rho_{fiber} + (1-f) \cdot \rho_{matrix} \tag{8}$$

The layer properties are listed in Table 2, and Tsai's modulus (*TM*) [34] can be calculated using Equation (9). This parameter is constant for all stacking sequences built using this material.

$$TM = Q_{11} + Q_{22} + 2 \cdot Q_{66} = 52.3\ GPa \tag{9}$$

The values of the stiffness parameters Q_{11}, Q_{22}, and Q_{66} can be calculated using Equations (10)–(12), respectively, depending on the theoretical UD layer mechanical properties.

$$Q_{11} = \frac{E_1}{\frac{E_1 - \nu_{12}^2 \cdot E_2}{E_1}} \tag{10}$$

$$Q_{22} = \frac{E_2}{\frac{E_1 - \nu_{12}^2 \cdot E_2}{E_1}} \tag{11}$$

$$Q_{66} = G_{12} \tag{12}$$

The Tsai normalized modulus in the fiber direction (NM_1) is expressed in Equation (13).

$$NM_1 = \frac{E_1}{T_M} = 0.69\ GPa \tag{13}$$

These values are in the range of the reported values for glass fibers laminates [35].

The obtained theoretical unidirectional layer properties were implemented in a laminate comprising four individual layers at 0° and 90° with a symmetrical distribution for the determination of in-plane mechanical properties using classical laminate theory.

Each theoretical layer can be treated as an orthotropic material, and the relationship between the strain $\boldsymbol{\varepsilon}$ and stress $\boldsymbol{\sigma}$ for the layer can be expressed using Equation (14).

$$\boldsymbol{\varepsilon} = \mathbf{C} \cdot \boldsymbol{\sigma} \tag{14}$$

where $\mathbf{C}$ denotes the compliance matrix of the constitutive equation. In lamination theory, the strain in any layer can be defined as the sum of the mid-surface strain $\{\boldsymbol{\varepsilon}_0\}$ and the product of curvature $\{\boldsymbol{\kappa}\}$ and the distance from the midsurface, as expressed in Equation (15).

$$\boldsymbol{\varepsilon} = \boldsymbol{\varepsilon}_0 + z \cdot \boldsymbol{\kappa} \tag{15}$$

Furthermore, it is typical to work with the stress and moment resultants in the thickness direction, as expressed in Equation (16).

$$\begin{Bmatrix} \boldsymbol{\varepsilon}_0 \\ \boldsymbol{\kappa} \end{Bmatrix} = \begin{bmatrix} \mathbf{a} & \mathbf{b} \\ \mathbf{b} & \mathbf{d} \end{bmatrix} \begin{Bmatrix} \mathbf{N} \\ \mathbf{M} \end{Bmatrix} \tag{16}$$

The force $\{\mathbf{N}\}$ and moment $\{\mathbf{M}\}$ vector resultant per unit length were calculated according to Equations (17) and (18).

$$\mathbf{N} = \int_{-h}^{h} \boldsymbol{\sigma} \cdot dz, \tag{17}$$

$$\mathbf{M} = \int_{-h}^{h} \boldsymbol{\sigma} \cdot z \cdot dz, \tag{18}$$

where the total laminate thickness is 2 h and the mid-surface is placed at z = 0.

From the compliance matrix defined in Equation (16) (the fully expanded form is included in the material parameter calculation in Appendix B), the effective in-plane mechanical properties were obtained considering the total laminate thickness (2 h) using Equations (19)–(22).

$$E_x = \frac{1}{2h \cdot a_{11}} \tag{19}$$

$$E_y = \frac{1}{2h \cdot a_{22}} \tag{20}$$

$$\nu_{xy} = -\frac{a_{12}}{a_{11}} \tag{21}$$

$$G_{xy} = \frac{1}{2h \cdot a_{66}} \tag{22}$$

where E_x and E_y are respectively the Young's moduli in the laminate X and Y directions, ν_{xy} and ν_{yx} are the major and minor Poisson's ratios, respectively, and G_{yx} is the shear in-plane shear modulus.

For 3D analysis, the out-of-plane mechanical properties can be evaluated using the average value between theoretical layers considering the transformation of the three-dimensional compliance matrix to the laminate direction (Equation (23)). Fully expanded compliance and transformation matrices can be found in Appendix B (material parameter calculation).

$$\overline{\mathbf{C}} = \mathbf{T}^{\mathbf{T}} \cdot \mathbf{C} \cdot \mathbf{T} \tag{23}$$

The out-of-plane Young's modulus E_z, shear modulus G_{yz} and G_{xz}, and Poisson ratios ν_{yz} and ν_{xz}, for the layer were calculated using Equations (24)–(28).

Table 3
Mechanical properties of TEPEX PA6/47 102 layer calculated using ampliated lamination theory.

Density (kg/m^3)	1800
E_x (MPa)	23 000
E_y (MPa)	23 000
E_z (MPa)	9380
G_{xy} (MPa)	2780
G_{xz} (MPa)	2980
G_{yz} (MPa)	2980
ν_{xy}	0.12
ν_{xz}	0.36
ν_{yz}	0.36

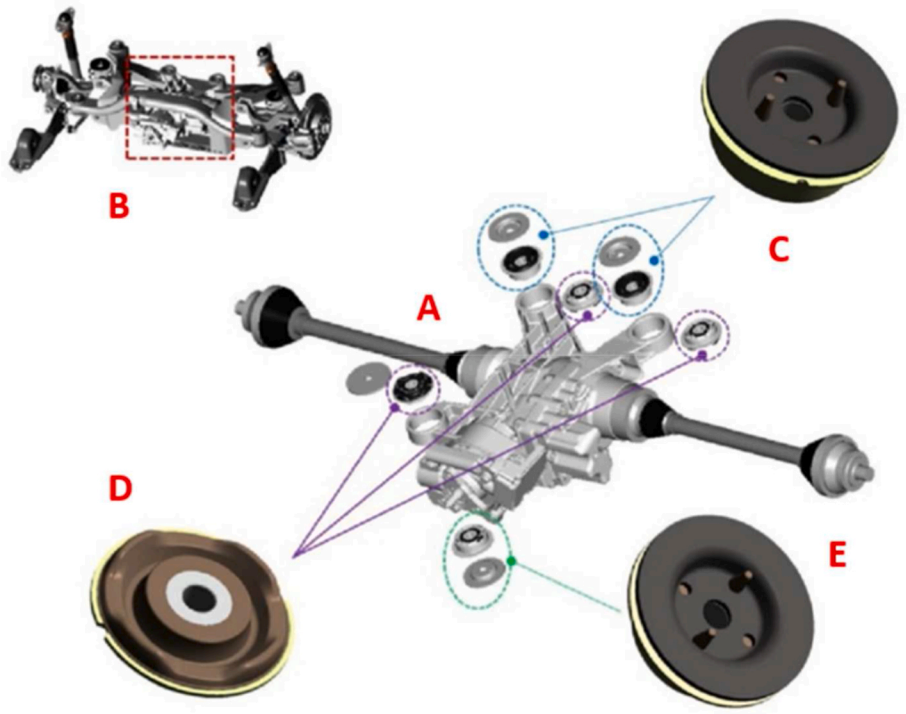

Fig. 5. Schematic of differential system (A) integrated into automobile steering system (B). Magnified view of antivibration top-mount connections to chassis (C) and components. Central top cover (E) and lower support (D).

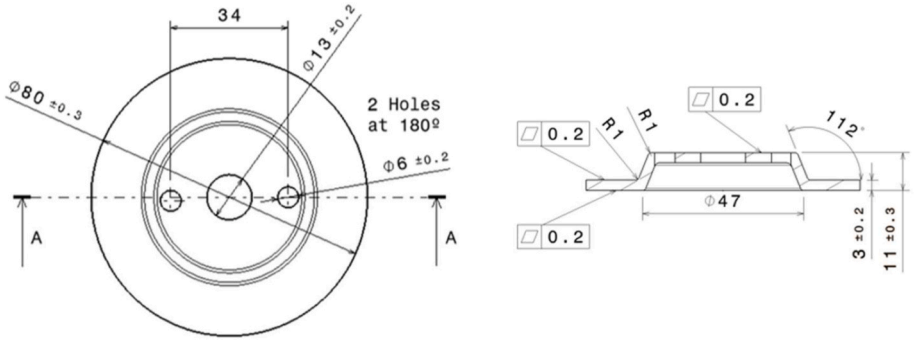

Fig. 6. Dimensions (mm) of the CFRTPs central cover of the fabricated top mount.

Table 4
Thermoforming parameters implemented for central top cover manufacturing.

Heating temperature (°C)	260
Mold temperature (°C)	110
Transportation time (s)	3
Approach Speed of the press (mm/s)	50
Forming velocity (mm/s)	5
Forming Pressure (bar)	5
Demolding temperature (°C)	110
Time to demolding (s)	20
Cycle time (s)	40

$$E_z = \frac{2h}{\sum_{i=1}^{n} t_i . C_{33}^i} \tag{24}$$

$$G_{yz} = \frac{2h}{\sum_{i=1}^{n} t_i . C_{44}^i} \tag{25}$$

$$G_{xz} = \frac{2h}{\sum_{i=1}^{n} t_i . C_{55}^i} \tag{26}$$

$$\nu_{yz} = \frac{2h}{\sum_{i=1}^{n} t_i . \left(- \frac{C_{11}^i}{C_{13}^i} \right)} \tag{27}$$

$$\nu_{xz} = \frac{2h}{\sum_{i=1}^{n} t_i . \left(- \frac{C_{22}^i}{C_{23}^i} \right)} \tag{28}$$

where t_i is the individual layer thickness and C_{jk}^i parameters are the global compliance parameters for each layer.

Considering that each tape of TEPEX PA6/47 102 comprises a symmetrical laminate of layers at 0° and 90° with equal individual thicknesses, the obtained mechanical properties are listed in Table 3. The Tsai normalized modulus (Equation (13)) in the x-and y-directions is $NM_y = NM_y = 0.44$, which is in the range of reported values [36].

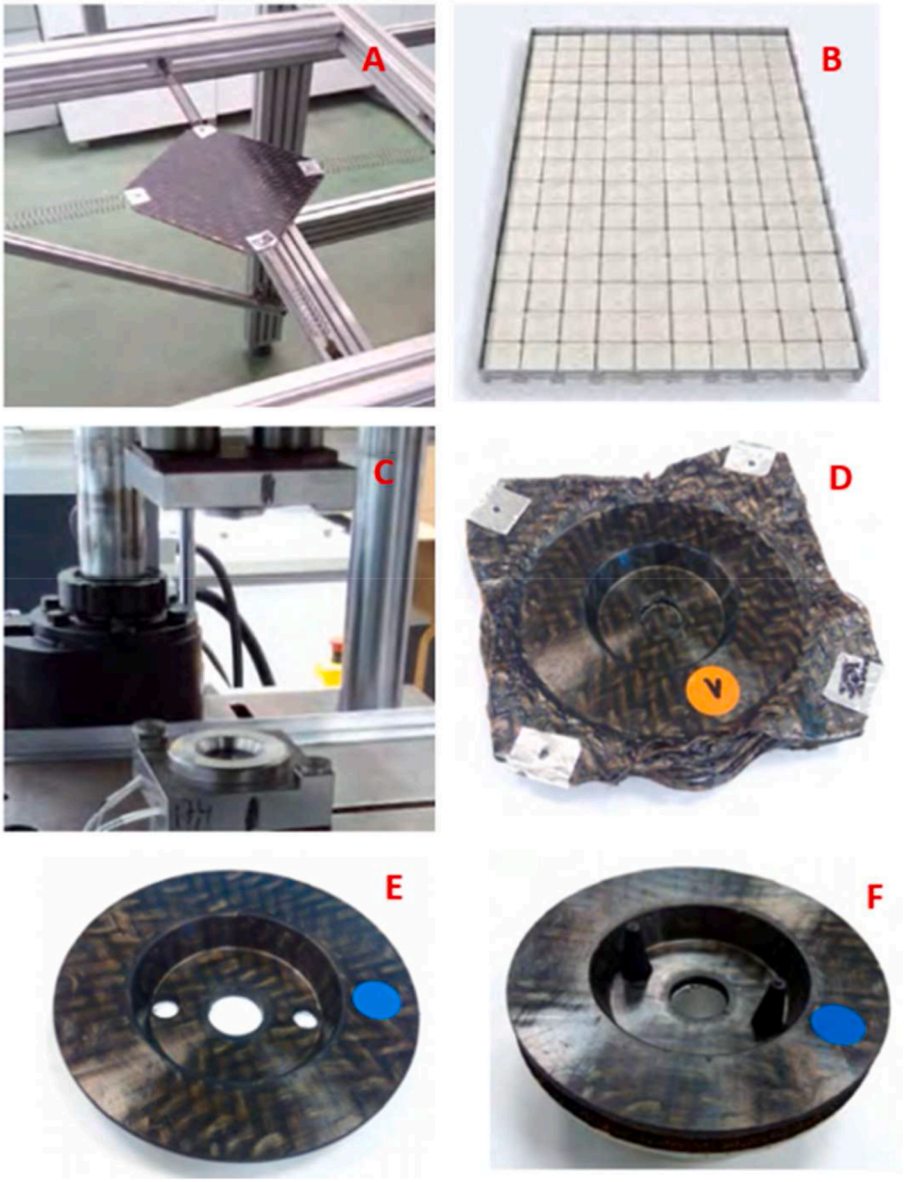

Fig. 7. Main step in the fabrication of the central cover top mount. Detail of laminate support (A), infrared lamps for heating process (B), thermoforming mold (C), thermoformed component (D), final machined central CFRTPs component (E), and final top mount assembly (F).

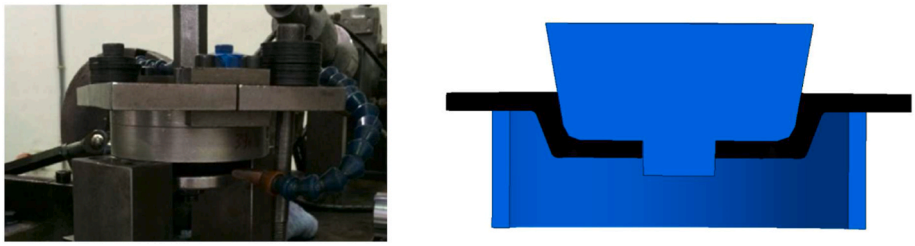

Fig. 8. Image of axial tooling (left) and assembly scheme (right) for axial tests. The main dimensions of the developed tooling component is shown in Fig. 9.

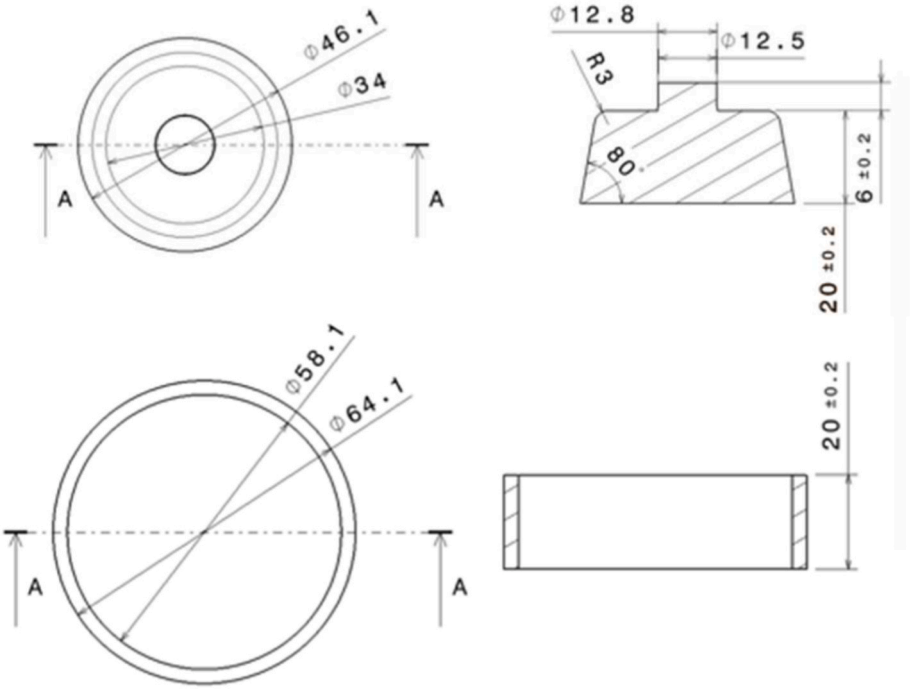

Fig. 9. Dimensions (mm) of the tooling component fabricated for axial tests. Lower support (top) and load application cylinder (bottom).

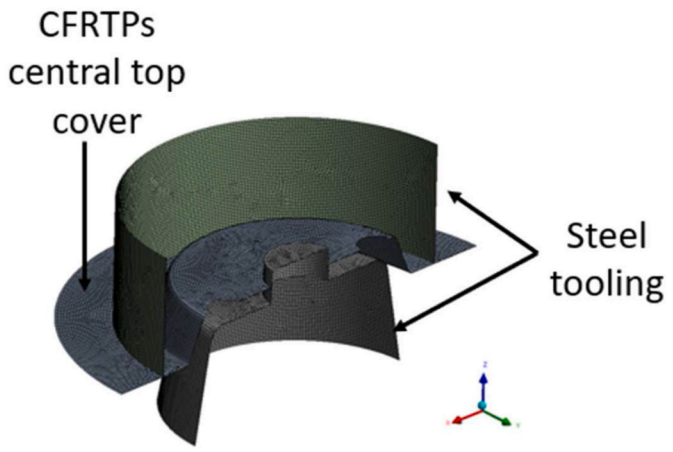

Fig. 10. Geometry of 2D symmetric FE model generated for central cover top mount analysis. Steel tooling (upper and lower components) and CFRTPs central top cover (central component).

2.4. Case study of a CFRTPs component

A standard steel central core cover of a differential gear mount (CMP Automotive Group S. L., La Rioja, Spain) was substituted with a CFRTPs component based on TEPEX PA6/47 102. The CFRTPs cover position and details are shown in Fig. 5. This component is integrated into the automobile steering system (B), allowing the wheels on the same axle to rotate at different speeds. The system was attached to the main structure using gear mounts (C). These elements are based on a metal-rubber assembly (D, E) connected to the chassis through bolted joints. Gear mounts reduce the vibration transmission to the main structure of the automobile. The use of CFRTP in the central core cover (E) was justified based on the results obtained in previous studies [5,7].

The dimensions of the fabricated CFRTPs components are shown in Fig. 6, wherein a radius of curvature of 1 mm is considered [37].

The central cover of the top mount was fabricated using a thermoforming process applied to six layers oriented in the same direction until a total thickness of 3 mm was reached. The thermoforming parameters were chosen from the average values obtained from the manufacturer's datasheet and previous work [38] (Table 4).

The fabrication process is illustrated in Fig. 7. The laminate built with layers of TEPEX PA6/47 102 material was supported in the corners by a bush system to hold the component fixed during the thermoforming process (Fig. 7A). The corners were protected with aluminum foil to guarantee the geometry during the heating process.

The heating process was performed with two panels of 76 infrared lamps heating the components on both sides, as shown in Fig. 7B. The lamps are of Elstein HTS/1-600-230 type, divided into 14 zones where the temperature is monitored with thermocouples. Panels were used to heat the layers on both the sides. The layer was loaded into the mold when the temperature reached 240 °C in less than 3 s and subjected to compaction pressure.

This step was carried out with an ad hoc mold specifically designed for application in which the layer is thermoforming with a compaction pressure of 4 bar (Fig. 7C). The resulting thermoforming central cover (Fig. 7D) was machined (Fig. 7E) to obtain the top mount assembly (Fig. 7F).

2.5. Axial test

The CFRTPs central cover of the top mount was tested with a specially designed tool (Fig. 8) that held the central cover top mount in a working position during loading of the composite component in the experiment. As the influence of bolted connections has already been analyzed [7], it was not considered in this study and only the bending behavior of the CFRTPs component was analyzed. The test was carried out at 23 °C with a cyclic load from 500 N to 24 000 N, increasing the load steeply.

The CFRTPs central cover top mount component was inserted into the base tooling and compressed with the cylinder. At each load step, the maximum vertical displacement and maximum permanent displacement after the load application were measured.

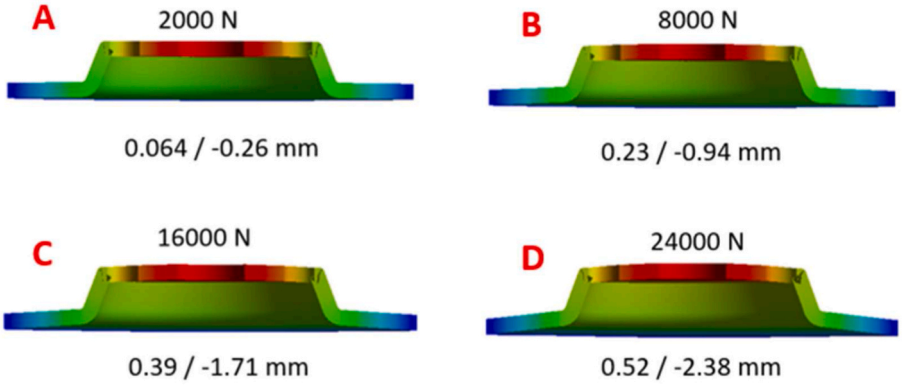

Fig. 11. Vertical displacements (mm) for axial test using CFRTPs central top cover for loads of 2000 N (A), 8000 N (B), 16 000 N (C) and 24 000 N (D). Upper direction (red zone)/Lower direction (blue zone). (For interpretation of the references to colour in this figure legend, the reader is referred to the Web version of this article.)

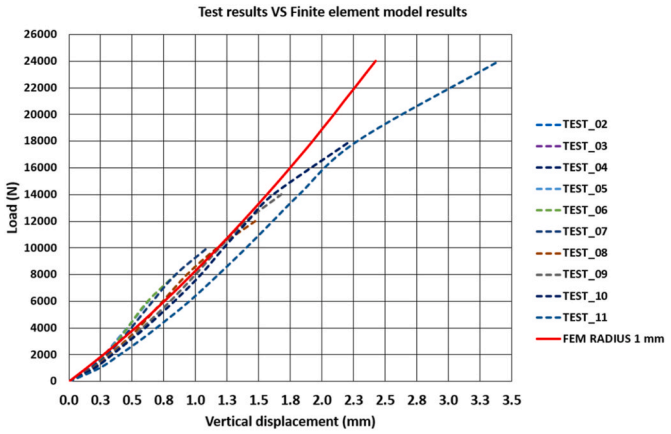

Fig. 12. Comparison of vertical displacements between test results (dashed lines for different tests) and FE results (solid red line) for central cover top mount (mm). (For interpretation of the references to colour in this figure legend, the reader is referred to the Web version of this article.)

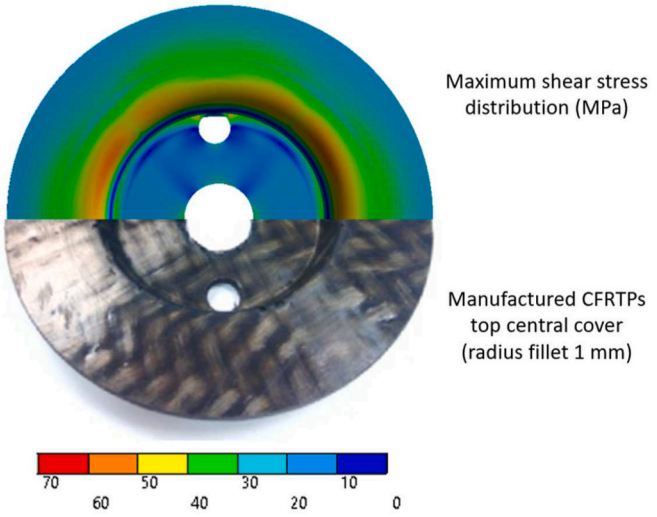

Fig. 13. Contour of the interlaminar shear stress for CFRTPs top central cover (top, MPa) for an axial load of 6000 N (material allowable stress is 64 MPa) and fabricated CFRTPs top central cover (bottom).

2.6. 2.6 simulation of the axial test

The axial tooling test components and central cover top mount were analyzed based on a FE simulation using the ANSYS software (Swanson Analysis System Inc., USA). A symmetric half model comprising 29 003 SHELL182 (2D) mesh elements was developed, considering the middle surfaces and component equivalent thickness (Fig. 9). The material was oriented using a local coordinate system.

Axial tooling (support and cylinder) was simulated with a steel material, whereas the central cover of the top mount was simulated considering an orthotropic material with the properties obtained previously for the material TEPEX PA6/47 102. In this study, the viscoelastic behavior associated with the polymer matrix was not simulated, and the equivalent material behavior was considered linear.

Mesh size convergence analysis was carried out until the maximum principal stress variation was less than 2%. A final mesh size of 0.5 mm was considered in this model, and frictional contact between components was defined considering a friction coefficient of 0.2.

Considering the global coordinate system shown in Fig. 10, displacements X, Y, and Z at the lower edge of the tooling component were constrained, whereas the upper edge of the cylinder was constrained in the X and Y directions. The rotation around the Z-axis was constrained to the central cover top mount component of the CFRTPs.

The load on the upper edge of the cylinder was increased from 1000 to 24 000 N in steps of 1000 N.

3. Results

The vertical displacements obtained using the FE model showed a non-linear evolution owing to the adjustment of the central cover top mount over the lower tooling component. The vertical displacement can be observed in representative images shown in Fig. 11. The central and perimetral zones exhibited upward and downward movements, respectively.

A comparison between the FE model and test results is shown in Fig. 12, considering the values of the FE model with a fillet radius of 1 mm (red line). Considering the average value obtained in the tests, the values obtained with the FE model showed an average difference of 0.021 mm with a standard deviation of 0.022 mm until a load of 10 000 N. However, the FE and test results diverged when the load exceeded this value. This could be associated with nonlinear effects in the CFRTPs component due to the beginning of interlaminar failure.

The test results exhibited an Shaped evolution curve, which could be explained by considering the following deformation process: at a low load level (lower than 500 N), the composite twill configuration, with

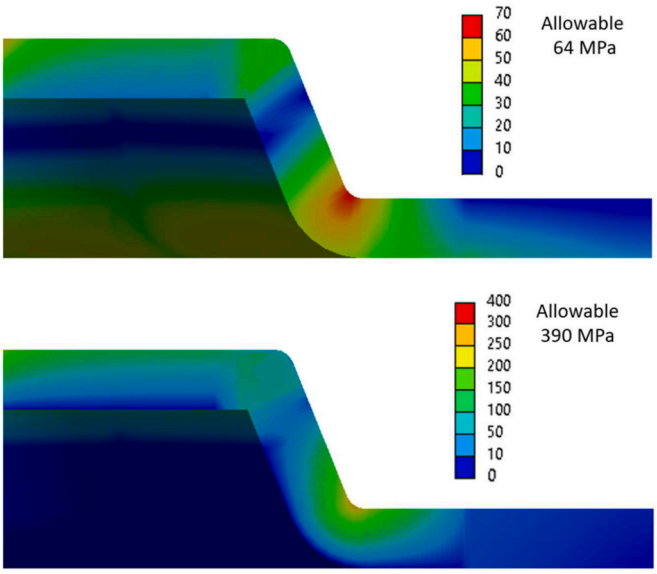

Fig. 14. Contours of maximum shear stress (MPa) (top) and maximum principal stress (MPa; bottom) for configuration with a fillet radius of 1 mm at an applied load of 6000 N.

fibers in an undulatory distribution, is elongated owing to the deformation of the matrix until the fibers reach a blocking configuration wherein the composite material behavior shows a change in the load displacement curve. Furthermore, the accommodation process between the components produces an extra displacement variation, as identified in the FE analysis results, which exhibit a non-linear behavior.

The non-linear evolution in the displacements in the FE model was due to the contact between the components. When the load was increased, the tooling component deformed the central cover of the top mount by varying the contact surface, the constraints imposed by the tooling on the composite component, and the effective bending length.

From the blocking configuration, the laminate exhibited a quasi-linear behavior. However, the slopes in the incremental load test were lower, according to the results obtained in Test 6. This can be attributed to the interlaminar shear failure in the external zone of the component in the lower fillet zone, as shown in Fig. 13, which shows the transverse shear stress for Test 6 with an applied load of 6000 N.

In this case, the maximum interlaminar shear strength of 64 MPa was achieved [39]. Crack initiation at the polymer fibers interface contributes to the delamination between the external layers and a worse behavior in further tests where a more flexible structure is obtained.

Although the maximum shear strength of the polymer matrix is reached in the external zone at axial loads of approximately 6000 N with crack initiation in the polymeric matrix, the values of the maximum principal strength obtained are lower than the maximum tensile of strength the material, and the composite structure can withstand the load. This is evident from Fig. 14, which shows the maximum principal stress for a load of 6000 N (bottom). It reached a value of 167 MPa, which is lower than the material allowable stress of 390 MPa.

After the validation of the material model by comparing the test results with those of the FE analysis (fillet radius of 1 mm), a new geometrical model was developed in which the fillet radius was increased to 5 mm to reduce the interlaminar stress concentration in the transition zone (Fig. 15).

Increasing the fillet radius allowed fibers to operate in a more optimized way, reducing the out-of-plane stress concentration in the transition zones (Fig. 16). The onset of the matrix crack initiation increased from 6000 N to 8000 N.

In addition to the displacement and stress analysis carried out using the fabricated components, the remnant displacement was evaluated in the axial test using the configuration with fillet radii of 1 mm and 5 mm (Fig. 17). The remnant displacement considers the viscous behavior of the thermoplastic matrix and can be included in the development of more accurate FE models with cycle hysteresis integration. Test results were used for the configuration with a fillet radius of 1 mm, whereas previous values were corrected by a factor for the configuration with a fillet radius of 5 mm. This factor considers the relationship between the maximum principal stress obtained in the fillet radius zone for both geometries. For equal loads, the remnant values for the configuration with a fillet radius of 5 mm were lower than those for the configuration with a fillet radius of 1 mm.

In this study, a maximum remanent displacement of 0.2 mm was considered. This value is based on the standard flatness tolerance requirements specified in ISO 2768–2 for ranges above 30–100 mm with a tolerance class K. The combination of the maximum remanent displacement for the flatness requirements and maximum load allowed to avoid interlaminar failure was used to define the working zone. The reduction in the stress concentration with the increment in the fillet radius allows an increment in the working zone.

4. Conclusions

The development of complex geometries made of continuous fiber-

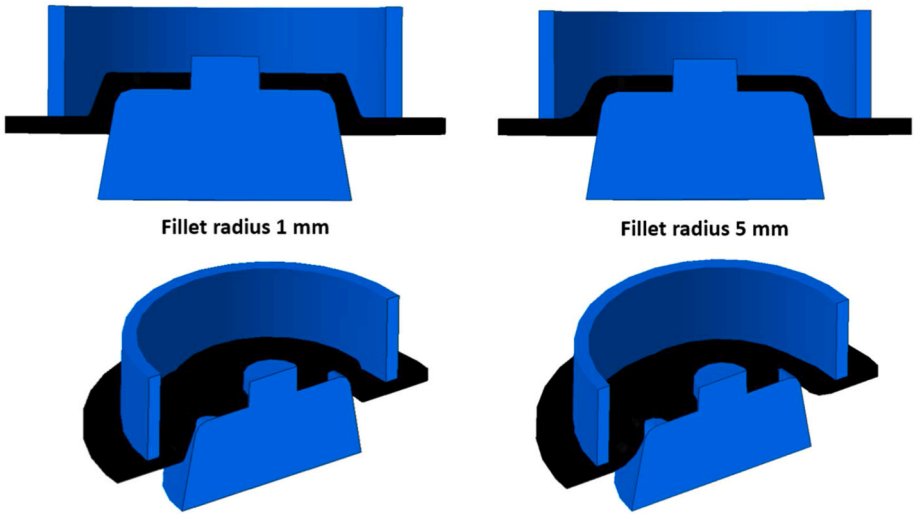

Fig. 15. Comparison between test configuration with fillet radius of 1 mm (left) and optimized configuration with fillet radius of 5 mm (right).

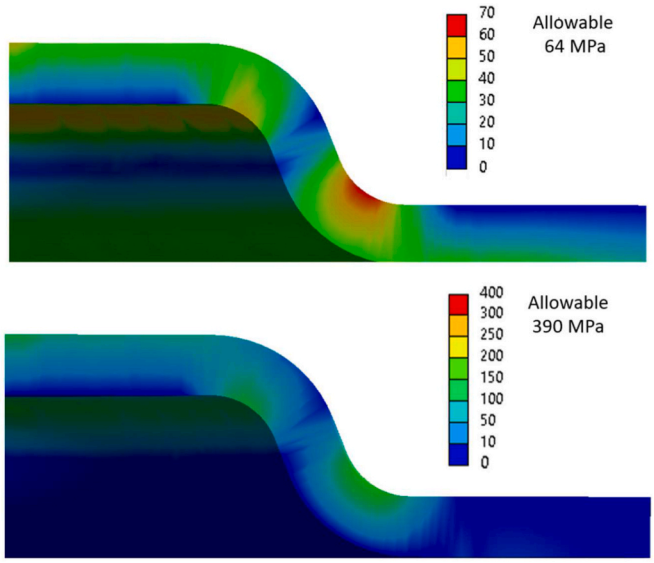

Fig. 16. Contours of maximum shear stress (MPa) (top) and maximum principal stress (MPa; bottom) for configuration with a fillet radius of 5 mm at an applied load of 8000 N.

reinforced thermoplastics (CFRTPs) can be optimized using finite element (FE) models. However, this is challenging because of the lack of information in material datasheets regarding the mechanical properties and strength. Addressing this problem requires the development of time-consuming and costly tests or theoretical calculations.

In this study, the mechanical moduli and Poisson's ratio for a commercial CFRTPs made of polyamide 6 reinforced with long glass fibers (47% in volume) were theoretically calculated based on the Halpin–Tsai model and 3D expanded classical lamination theory. The Young's modulus provided in the material datasheet was used to validate the results. Furthermore, the novel Tsai's modulus (composite trace) and normalized modulus were calculated, and the values were within the range of known materials.

In addition, the mechanical damping behavior of the fabricated CFRTPs top mount for an automobile differential system was tested using specially designed ad hoc tooling. The results were used to those obtained using FE simulation involving models of tooling and CFRTPs.

The obtained results indicated that the geometry cannot be directly adapted from the metal component because of the interlaminar stress concentration in the fillet zone, where the allowable material reaches a low load level.

The geometry of the top damping component of the CFRTPs was optimized using FE analysis, wherein the fillet radius was increased. This modification resulted in an increase in the load bearing capacity of the component, delaying the out-of-plane failure in the fillet zone and increasing the working zone defined for this component with the load limitation and flatness tolerance based on ISO 2768–2.

In summary, the use of CFRTPs can contribute to a considerable weight reduction in automobile components and lower greenhouse gas emissions without diminishing the reliability and safety throughout their useful life. Furthermore, their excellent dielectric and isolation properties can facilitate the incorporation of electronic devices with new functionalities in the automotive industry [40].

The use of in silico models based on FE techniques can be useful for accelerating the development of complex structures made of recycled CFRTPs for large-scale production.

Future research could include the analysis of thermoforming parameters and the influence of hydrothermal degradation in the polymeric matrix [41] to optimize the mechanical performance and life of the part, which was not considered in this study.

Credit author statement

C. Gómez: Conceptualization, Formal analysis, Methodology, Resources, Software, Validation, Writing - original draft. D. Tobalina-Baldeon: Data curation, Formal analysis, Investigation, Resources, Writing - original draft. F. Cavas: Conceptualization, Investigation, Project administration, Validation, Visualization, Writing - original draft, Writing - review & editing. F. Sanz-Adan: Conceptualization, Investigation, Project administration, Supervision, Writing - original draft, Writing - review & editing.

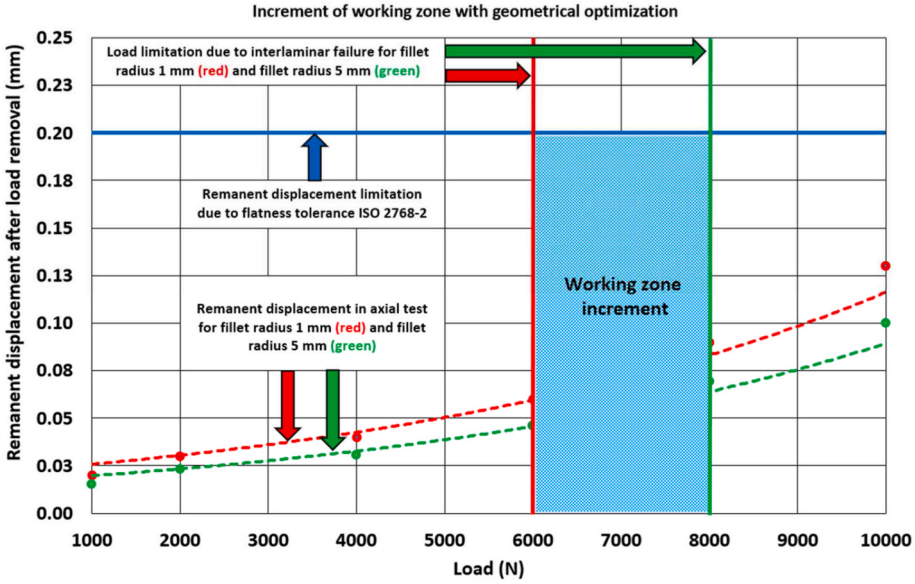

Fig. 17. Influence of geometrical optimization on the working zone increment. Load limitation and remnant displacement with fillet radii of 1 mm (red line) and 5 mm (green line) Standard flatness tolerance (blue line). (For interpretation of the references to colour in this figure legend, the reader is referred to the Web version of this article.)

Declaration of competing interest

The authors declare that they have no known competing financial interests or personal relationships that could have appeared to influence the work reported in this paper.

Acknowledgments

The authors would like to acknowledge the support of CMP Automotive Group for collaboration in the experimental part and to IGESTEK for the information provided on the composites it manufactures.

Appendix A. Supplementary data

Supplementary data to this article can be found online at https://doi.org/10.1016/j.compositesb.2022.109950.

References

[1] Pavlovic J, Clairotte M, Konstantinos A, Arcidiacono V, Fontaras G, Biagio C. Characterisation of real-world CO2 variability and implications for future policy instruments. 2017.
[2] Dandekar CR, Shin YC. Modeling of machining of composite materials: a review. Int J Mach Tool Manufact 2012;57:102–21.
[3] Gameros A, Lowth S, Axinte D, Nagy-Sochacki A, Craig O, Siller HR. State-of-the-art in fixture systems for the manufacture and assembly of rigid components: a review. Int J Mach Tool Manufact 2017;123:1–21.
[4] Hou W, Xu X, Sang L, Tong L. Failure of single hat-shaped thin-walled tubular composite T-joints under impact loading. Thin-Walled Struct 2020;154.
[5] Tobalina-Baldeon D, Sanz-Adan F, Martinez-Calvo MA, Santamaría-Pena J. Dynamic tensile stress-compressive stress behavior of thermoplastic matrix composite materials reinforced with continuous fiber for automotive damping and anti-vibration structural elements. Materials 2020;13(1):1–16.
[6] Tobalina-Baldeón D, Sanz-Adan F. Characterization of an adhesive bonding between continuous fiber reinforced thermoplastic (CFRTP) composites and vulcanized rubber under a shear load. Dyna 2019;94(3):226–32.
[7] Tobalina-Baldeon D, Sanz-Adán F, Martinez-Calvo M, Gómez C, Sanz-Pena I, Cavas F. Feasibility analysis of bolted joints with composite fibre-reinforced thermoplastics. Polymers 2021;13(12).
[8] Tsai SW. Double–double: new family of composite laminates. AIAA J 2021;59(11):4293–305.
[9] Kim D-H, Kim H-G, Kim H-S. Design optimization and manufacture of hybrid glass/carbon fiber reinforced composite bumper beam for automobile vehicle. Compos Struct 2015;131:742–52.
[10] Gong Y, Huang T, Zhang X, Suo Y, Jia P, Zhao S. Multiscale Analysis of mechanical properties of 3D orthogonal woven composites with randomly distributed voids. Materials 2021;14(18).
[11] Ishikawa T, Amaoka K, Masubuchi Y, Yamamoto T, Yamanaka A, Arai M, et al. Overview of automotive structural composites technology developments in Japan. Compos Sci Technol 2018;155:221–46.
[12] Malpot A, Touchard F, Bergamo S. Effect of relative humidity on mechanical properties of a woven thermoplastic composite for automotive application. Polym Test 2015;48:160–8.
[13] Chen L, Deng T, Zhou H, Huang Z, Peng X, Zhou H. A numerical simulation method for the one-step compression-stamping process of continuous fiber reinforced thermoplastic composites. Polymers 2021;13(19).
[14] Zhang H, Yan B, Gong Y, Xu Y, Peng X, Peng F. A lamination model for thermostamping of carbon woven fabric reinforced thermoplastic resin composites. Fuhe Cailiao Xuebao/Acta Materiae Compositae Sinica. 2017;34(12):2741–6.
[15] Zhang J, Taylor T, Kizaki T, Yanagimoto J. Bendable metal-based composite sheets with a truncated dome core made of carbon fibre reinforced thermoplastics. Composite Structures; 2020. p. 236.
[16] Bolt S. Ultrasonic plastic welding of carbon fiber reinforced Polyamide 6 to aluminum and Steel. 2014.
[17] Suzuki K, Ohsawa I, Takahashi J, Uzawa K. Numerical study on ultrasonic welding joint for CFRTP. ICCM International Conferences on Composite Materials. 2013. p. 9128–9.
[18] Zhang Z, Shan J, Tan X, Zhang J. Improvement of the laser joining of CFRP and aluminum via laser pre-treatment. Int J Adv Manuf Technol 2017;90(9–12):3465–72.
[19] Scarselli G, Quan D, Murphy N, Deegan B, Dowling D, Ivankovic A. Adhesion improvement of thermoplastics-based composites by atmospheric plasma and UV treatments. Appl Compos Mater 2021;28(1):71–89.
[20] Galińska A. Mechanical joining of fibre reinforced polymer composites to metals—a review. Part i: bolted joining. Polymers 2020;12(10):1–48.
[21] Galińska A, Galiński C. Mechanical joining of fibre reinforced polymer composites to metals-A review. Part II: riveting, clinching, non-adhesive form-locked joints, pin and loop joining. Polymers 2020;12(8).
[22] Hiken A. The evolution of the composite fuselage - a manufacturing perspective. SAE International Journal of Aerospace 2017;10.
[23] Kamble M, Shakfeh T, Moheimani R, Dalir H. Optimization of a composite monocoque chassis for structural performance: a comprehensive approach. J Fail Anal Prev 2019;19.
[24] Vermes B, Tsai SW, Massard T, Springer GS, Czigany T. Design of laminates by a novel "double–double" layup. Thin-Walled Struct 2021;165:107954.
[25] Tsai SW. Composite double-double and grid/skin structures. 2019.
[26] Tanaka K, Kitano T, Kawaguchi M, Watanabe K, Katayama T. Effect of stacking sequence on stiffness of Al/CFRTP multi-material hat shaped member and its cost evaluation. Zairyo/Journal of the Society of Materials Science, Japan. 2021;70(10):773–80.
[27] Saba N, Jawaid M, Sultan MTH. 1 - an overview of mechanical and physical testing of composite materials. In: Jawaid M, Thariq M, Saba N, editors. Mechanical and physical testing of biocomposites, fibre-reinforced composites and hybrid composites. Woodhead Publishing; 2019. p. 1–12.
[28] Van de Velde K, Kiekens P. Thermoplastic polymers: overview of several properties and their consequences in flax fibre reinforced composites. Polym Test 2001;20(8):885–93.
[29] Martynova E, Cebulla H. Chapter 7 - glass fibers. In: Mahltig B, Kyosev Y, editors. Inorganic and composite fibers. Woodhead Publishing; 2018. p. 131–63.
[30] Shrivastava A. 4 - additives for plastics. In: Shrivastava A, editor. Introduction to plastics engineering. William Andrew Publishing; 2018. p. 111–41.
[31] Halpin JC, Tsai SW. Effects of environmental factors on composite materials. Air Force Technical Report AFML-TR-67-423. 1969. Wright Aeronautical Labs, Dayton.
[32] Hull D, Clyne TW. An introduction to composite materials. 2 ed. Cambridge: Cambridge University Press; 1996.
[33] Hewitt RL, De Malherbe MC. An approximation for the longitudinal shear modulus of continuous fibre composites. J Compos Mater 1970;4(2):280–2.
[34] Arteiro A, Sharma N, Melo JDD, Ha SK, Miravete A, Miyano Y, et al. A case for Tsai's Modulus, an invariant-based approach to stiffness. Compos Struct 2020;252:112683.
[35] Tsai SW, Sihn S, Melo J. Trace-based stiffness for a universal design of carbon-fiber reinforced composite structures. Compos Sci Technol 2015;118:23–30.
[36] Tsai S, Sharma N, Arteiro A, Roy S, Rainsberger B. Composite double-double and grid/skin structures. 2019.
[37] Dequine D, Howell D, Cramer D, Lizotte AM. A novel stamp forming technique for crush-resistant stringers made of thermoplastic composites. 2012.
[38] Fiorotto M, Lucchetta G. Experimental investigation of a new hybrid molding process to manufacture high-performance composites. Int J Material Form 2013;6:179–85.
[39] Beier U, Sandler J, Altstädt V, Spanner H, Weimer C. Mechanical performance of carbon fibre-reinforced composites based on stitched and bindered preforms. Compos Appl Sci Manuf 2009;40:1756–63.
[40] Gómez C, Mira J, Carrión-Vilches FJ, Cavas F. Dynamic moduli of polybutylene terephthalate glass fiber reinforced in high-temperature environments. Materials 2021;14(3):1–13.
[41] Pivdiablyk I, Rozycki P, Jacquemin F, Gornet L, Auger S. Experimental analysis of mechanical performance of glass fibre reinforced polyamide 6 under varying environmental conditions. Compos Struct 2020;245:112338.